



Provided by the author(s) and University of Galway in accordance with publisher policies. Please cite the published version when available.

Title	Stability enhancement of an atomic force microscope for long-term force measurement including cantilever modification for whole cell deformation
Author(s)	McGarry, J. Patrick; Weafer, Paul; Ronan, William; Nolan, D. R.
Publication Date	2012
Publication Information	Weafer, PP, McGarry, JP, van Es, MH, Kilpatrick, JI, Ronan, W, Nolan, DR, Jarvis, SP (2012) 'Stability enhancement of an atomic force microscope for long-term force measurement including cantilever modification for whole cell deformation'. Review Of Scientific Instruments, 83 .
Link to publisher's version	http://dx.doi.org/10.1063/1.4752023
Item record	http://hdl.handle.net/10379/4113
DOI	http://dx.doi.org/http://dx.doi.org/10.1063/1.4752023

Downloaded 2024-04-25T13:50:44Z

Some rights reserved. For more information, please see the item record link above.



Stability enhancement of an atomic force microscope for long-term force measurement including cantilever modification for whole cell deformation

P. P. Weafer,¹ J. P. McGarry,^{1,a} M. H. van Es,² J. I. Kilpatrick,² W. Ronan,¹ D. R. Nolan¹ and S. P. Jarvis^{2,a}

¹*Department of Mechanical and Biomedical Engineering, National University of Ireland, Galway, Ireland*

²*Nanoscale Function Group, Conway Institute of Biomolecular and Biomedical Research, University College Dublin, Ireland*

Atomic force microscopy (AFM) is widely used in the study of both morphology and mechanical properties of living cells under physiologically relevant conditions. However, quantitative experiments on timescales of minutes to hours are generally limited by thermal drift in the instrument, particularly in the vertical (z) direction. In addition, we demonstrate the necessity to remove all air-liquid interfaces within the system for measurements in liquid environments, which may otherwise result in perturbations in the measured deflection. These effects severely limit the use of AFM as a practical tool for the study of long term cell behavior, where precise knowledge of the tip-sample distance is a crucial requirement. Here we present a readily implementable, cost effective method of minimizing z -drift and liquid instabilities by utilizing active temperature control combined with a customized fluid cell system. Long term whole cell mechanical measurements were performed using this stabilized AFM by attaching a large sphere to a cantilever in order to approximate a parallel plate system. An extensive examination of the effects of sphere attachment on AFM data is presented. Profiling of cantilever bending during substrate indentation revealed that the optical lever assumption of free ended cantilevering is inappropriate when sphere constraining occurs, which applies an additional torque to the cantilevers 'free' end. Here we present the steps required to accurately determine force-indentation measurements for such a scenario. Combining these readily-implementable modifications, we demonstrate the ability to investigate long term whole cell mechanics by performing strain controlled cyclic deformation of single osteoblasts.

^a) Electronic mail: suzi.jarvis@ucd.ie; patrick.mcgarry@nuigalway.ie

I. INTRODUCTION

Studies have shown that cells readily align in response to cyclic substrate stretching.^{1,2} However, changes in the stretching force applied to the cell due to cellular remodeling and associated changes in the active contractility of the actin cytoskeleton have not been reported for such studies. Force measurement has been implemented in macroscale experiments whereby cell seeded collagen scaffolds were cyclically stretched at constant strain rates.³ The active contribution of the cells was isolated and it was demonstrated that lower strain rates resulted in higher steady state forces following several hours of cyclic deformation. This behavior cannot be explained by standard passive viscoelastic material models which predict higher stresses at higher strain rates. A recent computational investigation of the response of cells to cyclic stretching using an active bio-chemo-mechanical model suggests a link between dissociation of the actin cytoskeleton and reduction in cellular tension during cyclic loading.⁴ This model provides an explanation of the strain rate effects observed by Wille *et al.*³ However, in order to validate this theory, strain controlled cyclic deformation must be applied to single cell studies whereby the resultant forces are measured and the corresponding cell remodeling visualized over a physiologically relevant time period.

In this paper, we present the modifications required to adapt an atomic force microscope (AFM) to perform such a study. Using the modified system described here, the goal is to apply strain controlled uniform loading of the whole cell while measuring forces generated at a single cell level. AFM is an ideal candidate due to the significant force resolution and displacement precision available. Pico-Newton scale force measurements at sub-nanometer displacement precision can routinely be obtained. This is in comparison to other deformation systems where the accuracy of force measurement is in the range of 1-10 nN.^{5,6,7}

AFM has been used extensively for measurements of single cell mechanics over timescales ranging from seconds to minutes; however, issues arise when measurements are performed over longer timescales. Here we demonstrate that uncertainties in the tip-sample distance, which are due to thermal drift (z-drift) will, if uncorrected, introduce significant errors in AFM measurement of single cells over longer timescales. It is also demonstrated in the current paper that perturbations in the z-axis due to instabilities associated with liquid motion (liquid instability), may impose severe limitations in the application of AFM over large timescales, the extent of which is often not fully considered. The elimination of both z-drift and liquid instabilities is critical for experiments in which precise, uninterrupted control of applied cell deformation, and corresponding force measurement, must be achieved over long timescales. Combined with a customized fluid cell system, we demonstrate displacement controlled operation in liquid environments over long timescales, without requiring direct modification of existing AFM instrumentation.

Previous drift related studies have primarily focused on thermal drift in the lateral (xy) plane for imaging purposes.^{8,9,10} Approaches including intermittent substrate referencing between force measurements¹¹ or the use of reference sensors^{12,13,14,15} can be applied to counteract, rather than prevent, thermal drift in the vertical direction (z-drift). However, intermittent substrate referencing is unsuitable when the cell dimensions exceed the lateral range of the AFM scanner or when continuous contact between the sphere and cell is a requirement. Also, reference sensor systems often require substantial modifications of existing instrumentation and great care must be taken to ensure that the sensor itself is inert to thermal effects. Customized systems have also been developed whereby thermal motion in one component counteracts thermal motion in another, resulting in an inherently stable instrument.^{16,17} Furthermore, there are several commercially available products designed specifically to manage thermal drift.^{18,19} Such systems represent significant advancements in

instrumentation but there is still a pressing need to develop a reliable, cost effective and easily implemented method of adapting any existing AFM for the purpose of long term displacement controlled experiments. Here we demonstrate such modifications without requiring direct modification of existing AFM instrumentation, which can be adapted to suit any conventional AFM system.

To highlight the importance of precise displacement control, whole cell cyclic deformation at a strain rate of 0.1 Hz was performed for both an unmodified and modified system. Whole cell deformation was achieved by attaching a $\text{\O}150\ \mu\text{m}$ sphere to the end of a tipless cantilever, the bottom of which acted as a planar surface for uniform loading, comparable to a parallel plate system. Examination of the cantilever bending profile revealed that the optical lever system assumption of free ended cantilevering is inappropriate when the sphere becomes constrained resulting in an additional torque being applied to the cantilevers leading edge. Here we present a practical methodology to correct such data in order to obtain the true force-indentation profile.

The modifications described within this paper enable displacement controlled AFM operation in liquid over long timescales which has great potential to be applied to other fields of research where long term stability is a requirement.

II. DISPLACEMENT CONTROLLED OPERATION

Before cell deformation experiments could be performed, it was first necessary to verify displacement control for a model system. Displacement controlled operation was initially achieved in air and then in a liquid environment, where the additional effects of liquid instability had to be accounted for.

A. Experimental design

Our goal was to minimize z-drift in the instrument without sacrificing system stability or incorporating any additional noise. Z-drift values are reported as the slope of a linear fit to 1 hour of z-displacement data and the relative noise in the system is indicated by the parameter z-sdev, which is the standard deviation of 1 hour of z-displacement data after subtracting the linear fit. By subtracting the fit from the data, a more accurate indication of system stability can be obtained since the impact of drift on this value is minimized. Here we define long term performance as z-drift and z-sdev over a 5 hour period as it approximates the time after which the cells used in this study are no longer viable on the AFM stage.

All work was performed using a MFP-3D AFM (Asylum Research, USA) combined with an Eclipse Ti microscope (Nikon, Japan). The system was positioned on a vibration isolation table (Micro 60, Halcyonics, Germany) and housed within a large acoustic isolation hood (BCH-45, Asylum Research, USA). Air conditioning maintained the lab temperature at 21 ± 1 °C.

Measurements were performed by monitoring the z-displacement required to maintain a constant force (≈ 60 nN) on a rigid substrate (Z integral gain = 1.0) in response to the deflection of a cantilever (Lever C, NSC36/AIBS, $k \approx 0.6$ N/m, MikroMasch, Spain). Temperatures were recorded using a USB-TC (Measurement Computing, USA) via Igor Pro (Wavemetrics, USA) by custom software at 5 discrete locations on the AFM (K-type thermocouples, Radionics, Ireland). All temperature and z-displacement data were collected using a sampling rate of 1 Hz unless otherwise stated. The acoustic isolation hood doors were kept closed during all experiments unless stated otherwise. All measurements were performed from the same initial system configuration ('cold system') defined as having the hood doors closed, the inverted microscope powered off and AFM controller on with the laser off for a period of 10 hours.

A TempControl 37-2 digital controller and heating unit (Zeiss, Germany) was used in experiments where active temperature control was required. The temperature control unit was mechanically isolated from the AFM system to suppress acoustic and vibration noise. An operating temperature of 35°C was chosen such that the instrument was kept above room temperature to reduce the influence of external temperature fluctuations whilst keeping below the maximum operating temperature of 40 °C specified by the instrument manufacturers. This temperature is also close to the optimal temperature of 37 °C for mammalian cells which extends the viability of the sample on the AFM stage. We define the system as a ‘warm system’ when thermal stability is reached.

B. Measurements in air

To elucidate the magnitude of z-drift under standard operating conditions (without active temperature control) measurements were performed on a glass slide in air over a period of 18 hours, Figure 1. Starting from a ‘cold system’, the laser and inverted microscope were powered on and temperatures within the isolation hood were observed to rise due to thermal dissipation. An offset was observed between thermocouple locations however, the rate of temperature increase was similar for all positions (data not shown). The AFM head temperature increased to a maximum value of 33.04 °C. After 5 hours of equilibration the temperature was 32.62 ± 0.31 °C with a linear rate of change of 0.09 ± 0.08 °C/hr.

Measurements were then repeated using a TempControl 37-2 digital controller and heating unit set to a value of 35 °C. The AFM head temperature increased to a maximum value of 35.51 °C. After 5 hours of equilibration the temperature was 35.28 ± 0.03 °C with a rate of change of 0.02 ± 0.02 °C/hr.

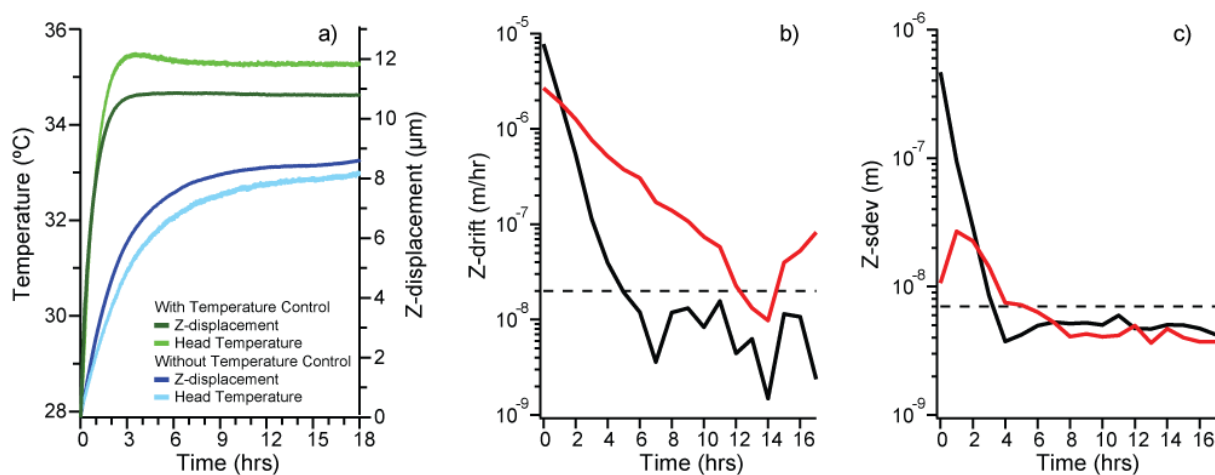


FIG. 1. a) AFM head temperature and measured z-displacement over 18 hrs with and without active temperature control. b) Z-drift with (black) and without (red) active temperature control. c) Z-sdev with (black) and without (red) active temperature control. For b) and c) increments of 1 hour were used for each data point. Dashed lines are included as indicators only and are defined as 20 nm/hr for b) and 7 nm for c).

After 5 hours of equilibration, the z-drift for the unmodified system was found to be 111.56 ± 112.97 nm/hr compared to 9.28 ± 5.41 nm/hr for the modified system, Figure 1b). This significant improvement in performance is primarily due to operating above the unmodified equilibration temperature of the system which negates the impact of slow variations in temperature due to instrument heat dissipation. There was no significant difference in system stability observed, with a z-sdev of 4.62 ± 1.08 nm for the unmodified system compared to z-sdev of 4.94 ± 0.46 nm for the modified system, Figure 1c). Minor adjustments such as laser positioning, AFM head and sample stage positioning were performed through the side portal window of the acoustic isolation hood. Such operations were not found to affect stability if performed in less than 1 minute.

Previous studies frequently state thermal equilibration times ranging from 60 minutes^{20,21} to several hours^{22,23}, however, it is clear from our results that substantially longer times may be required in order to reach thermal equilibrium in the absence of active temperature control. These results highlight the need for a more systematic approach to alleviating z-drift when conducting measurements over long time periods.

For the modified system, it was found that fully opening the acoustic isolation hood doors for 10 minutes required a period of 5 hours to reestablish stability (data not shown). As such, all major adjustments to samples and cantilevers were performed within a ten minute period, after which the system was left for 5 hours to re-equilibrate to a ‘warm system’.

For biological experiments under physiologically relevant conditions the addition of a fluid cell is required. As such, the performance of two fluid cells: a BioHeater™ fluid cell (Asylum Research, USA) and a glass bottomed petri dish (GBPD) (FluoroDish 50 mm, WRI, Florida) were also measured using a ‘warm system’ in air over a period of 5 hours for comparison, Figure 2.

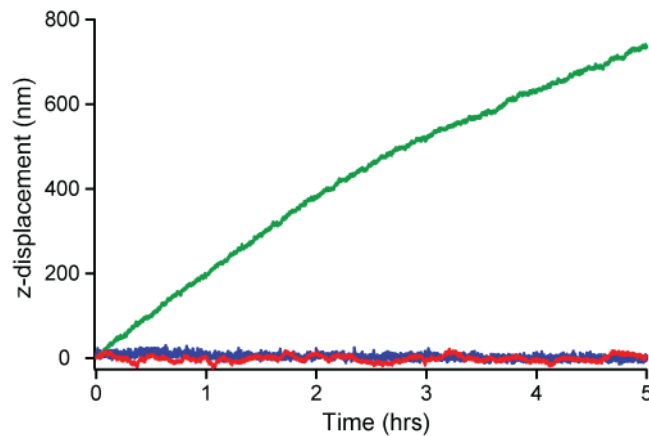


FIG. 2. Z-displacement in air using a ‘warm system’ on a glass slide (red) z -drift = 12.51 ± 5.26 nm/hr with z -sdev = 5.86 ± 0.52 nm, a GBPD (blue) z -drift = 2.98 ± 2.82 nm/hr with z -sdev = 4.90 ± 0.28 nm, and a BioHeater™ (green) z -drift = 148.37 ± 41.72 nm/hr with z -sdev = 3.37 ± 0.49 nm.

Best z -drift performance was found using the GBPD with a value of 2.98 ± 2.82 nm/hr compared to 12.51 ± 5.26 nm/hr for the glass slide and 148.37 ± 41.72 nm/hr for the BioHeater™. Again the stability of the system was found to be comparable in all cases. The origin of the high z -drift in the BioHeater™ system is unknown but may be attributed to the complexity of the design with a range of thermal expansion coefficients present (PEEK body, glass coverslip, O-ring, and a metal retaining ring). From these results, it is evident that the

GBPD has the lowest drift rate and so represented the best candidate for stable operation in liquid.

C. Measurements in liquid

Having demonstrated good stability in air the GBPD was then tested in liquid (phosphate buffered solution, PBS) using a ‘warm system’ over a period of 5 hours. With the GBPD open to the environment the system was unstable with changes in z-displacement of over 100 nm observed, Figure 3a). These perturbations are attributed to liquid movement arising from evaporation.

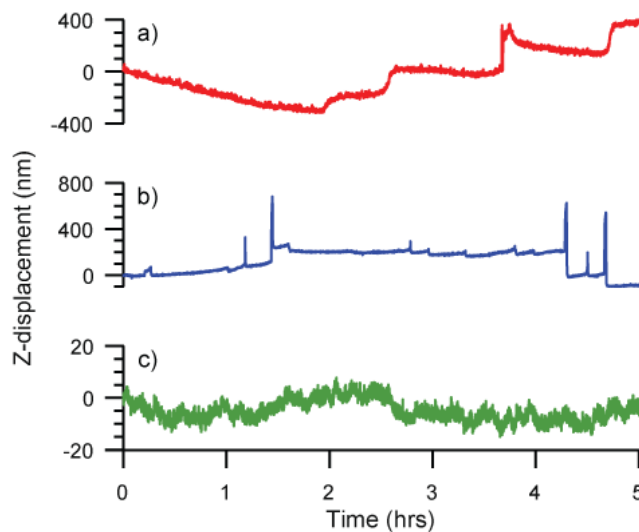


FIG. 3. Z-displacement using a ‘warm system’ in PBS of a) an open GBPD, b) customized closed fluid cell with trapped air, and c) customized closed fluid cell with all air expelled. Traces shown are representative of each condition (n=10).

Subsequently, a closed fluid cell was designed to minimize z-drift whilst maintaining system stability and additionally to provide; (a) the ability to inject cells/chemical agents into the fluid cell with minimal disruption, and (b) optical access from below to allow sample observation via confocal microscopy. Briefly, the closed fluid cell design (Figure 4) consists of a reservoir with an inlet tube (ID = 1 mm) containing a 3-way valve inserted into the side

of the GBP. The fluid cell itself was made up of a GBP with a flexible silicone membrane (Asylum Research, USA) clamped around the top circumference of the dish. This encapsulated the AFM cantilever holder within the fluid cell. The fluid cell was fixed to the AFM stage by a magnetic petri dish clamp assembly (Asylum Research, USA). A wider bore outlet tube (ID = 5 mm) exited the dish and finished within a second fluid reservoir.

Reservoirs were positioned such that the liquid levels (~125 ml) were the same in each reservoir. Each reservoir had an opening to allow for pressure equilibration during setup and cell/chemical injection through the 3-way valve. During experiments the valve was closed to eliminate liquid flow. By placing the reservoirs in the active temperature controlled hood thermal gradients within the fluid were also eliminated.

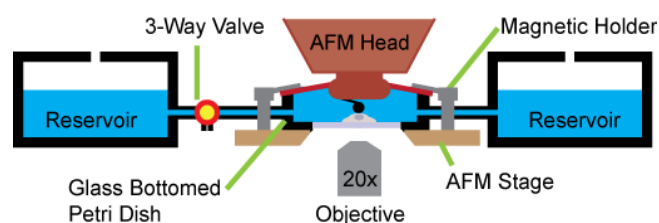


FIG. 4. Customized fluid cell; setup consists of a sealed GBP clamped to the AFM stage using a magnetic dish clamp assembly. The design is a closed system, air-free within the fluid cell. A 3-way valve is connected to an inlet tube to allow cell/chemical agent addition without further system restabilization.

Figure 3b) shows the performance of the customized fluid cell with trapped air present. For this system, liquid instabilities due to the trapped air resulted in sudden z-displacement jumps of hundreds of nanometers. Further investigation found that movement of trapped air (not removed during setup) or air bubbles formed (due to nucleation or when highly gas permeable tubing is used) within the system resulted in liquid instability ($n = 10$), see supplementary material.²⁴ The addition of even a small volume of air (0.008 cm^3) to the closed fluid cell resulted in instability. Therefore the use of gas impermeable tubing and bringing the liquid to system temperature prior to use was important. Additionally, prior to

experiments it was essential that air was completely expelled from the system. This was achieved by positioning the setup at such an angle that trapped air was forced through the system, exiting via the outlet tubing. Visual inspection of the transparent tubing and fluid cell verified the system remained air free. No liquid instability was observed when the fluid cell was assembled such that all air was expelled, Figure 3c).

Combining the customized closed fluid cell with active temperature control represents a practical method for obtaining displacement controlled AFM over long timescales with readily implementable modifications to any commercial system. The z-drift performance under physiologically relevant conditions was found to be 6.33 ± 3.90 nm/hr with a z-sdev of 2.40 ± 0.29 nm over a 5 hour period, Figure 3c). This represents a 17 fold improvement in z-drift and 2 fold improvement in system stability when compared to the operation of an unmodified AFM system in air. This combined with the ability to injecting cells via the side portal window of the acoustic isolation hood and using thermally equilibrated samples enables a displacement controlled system to be reestablished less than 10 minutes after injection.

III. CANTILEVER MODIFICATION FOR WHOLE CELL DEFORMATION

AFM based force spectroscopy is typically performed on localized regions of a cell using a cantilever with a nanoscale tip^{25,26} or by attaching a small colloidal sphere.^{27,28} This results in relatively localized measurements of cells, which are inhomogeneous by their nature. Furthermore, the application of uniformly distributed cell loading, using a standard AFM tipless cantilever is generally impractical due to its narrow geometry and angle of inclination (typically 10-15°). Therefore, AFM cantilever modifications are required where the application of a more uniform stress and strain field to a cell is a requirement. Here we present a method whereby we attach a large microsphere ($\text{\O} 150 \mu\text{m}$) to the end of a tipless

cantilever. The bottom of the sphere then forms the effective top planar surface for more uniformly distributed loading of the cell (for cell radius \ll sphere radius). The spheres used in this study are over 3 times larger than those used in previous studies, and as such provide a closer approximation to the planar surface assumption over the contact area and also allows for the investigation of larger cells.^{29,30}

Specifically, a \varnothing 150 μm glass microsphere (Whitehouse Scientific, UK) was attached to the end of a tipless cantilever (Lever F, NSC12/Tipless/AIBS, $k \approx 0.65$ N/m, MikroMasch, Spain). Cantilever deflection due to the weight of the sphere was calculated to be no greater than 1 μm post-attachment. Sphere attachment was performed using a two part epoxy (Loctite, Henkel Corp.) and a combined micro-manipulation/optical microscope setup. Scanning electron microscopy verified microsphere positioning on the leading cantilever edge post-attachment. The velocity of the cantilever during force curves was restricted to a maximum of 2 $\mu\text{m/s}$ in order to minimize any hydrodynamic force contribution.^{31,32}

A. Cantilever calibration

Quantitative AFM force measurements require the accurate calibration of the cantilever. For optical lever systems this involves calculating (i) the cantilever stiffness and (ii) optical lever sensitivity, OLS.

In the current study accurate calculation of the cantilever spring constant was not achievable using the thermal method³³ due to the additional mass of the attached sphere. Instead, the spring constant was determined after sphere attachment according to the added mass method proposed by Cleveland *et al.*³⁴ Spring constant values ranged from 0.3 - 0.5 N/m and were within ± 20 % of values obtained prior to sphere attachment via the thermal method.

OLS calibration is taken as the ratio of the change in voltage signal from the photodetector to the distance moved by the cantilever when pressed against a rigid substrate. The linear slope of the resulting voltage-displacement curve provides the OLS in units of V/nm. Friction between the sphere and substrate results in uncharacteristic voltage-displacement curves. As the sphere slides along the substrate, friction results in the loading and unloading sections of the curve often exhibiting a substantial hysteresis.^{35,36,37} Consequently, obtaining an accurate linear slope of the voltage-displacement curves can prove difficult. In this study, the mean of the slopes of the loading and unloading data was calculated as the best estimate of OLS, as previously reported by Chung *et al.*³⁶

It is important to note that even though optical lever measurements are usually reported as a deflection, it is the change in slope of the cantilever that is actually detected. When the cantilever deflects, the slope changes and this causes the laser to move across the detector.

B. Cantilever bending profiles: ‘sliding’ versus ‘constrained’

Application of the calibrated cantilever stiffness and OLS in order to obtain the applied force is only accurate when the cantilever behaves as a free ended cantilever. If friction between the sphere and substrate is sufficient to inhibit sphere sliding, the cantilever will no longer act as a free ended cantilever due to a rotation constraint at the cantilevers leading edge. Finite element simulations (Abaqus, Dassault Systemes, RI, USA) of cantilever loading were used to investigate this phenomenon. A cantilever, inclined at 11° , with a sphere attached to the leading edge was loaded against a rigid substrate until a $1\ \mu\text{m}$ deflection was achieved. Two cases were considered: (i) frictionless sliding of the sphere along the substrate, herein referred to as a ‘sliding sphere’ (Figure 5a)), and (ii) a ‘constrained sphere’ with no sliding permitted (Figure 5b)). The term *constrained sphere* is used in the following to

describe a sphere that does not slide along the substrate, leading to a rotational constraint on the end of the cantilever. Additionally, experimental SEM visualization of the deflection for sphere sliding (Figure 5c)) and sphere constraining (Figure 5d)) was performed using a modified sample stage. In Figure 5c) the sphere is free to slide along a glass substrate, whereas in Figure 5d) a point on the bottom of the sphere is fixed in space.

The finite element simulations and SEM images produced comparable results in which a clear difference in the cantilever bending profile between sphere sliding and constraining is evident. For the case of a sliding sphere, the bending profile is similar to that of a free ended cantilever (Figures 5a) and 5c)). For the constrained sphere, an additional torque is applied preventing rotation at the leading edge of the cantilever, so that the beam is essentially cantilevered at both ends (Figures 5b) and 5d)).

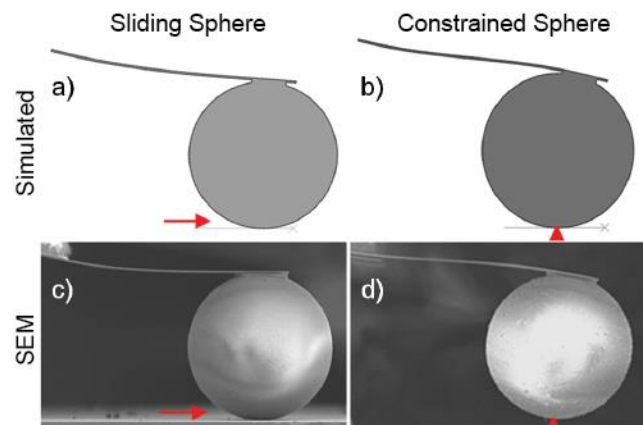


FIG 5. Finite element simulations (a, b) and SEM images (c, d) of a cantilever with a sliding and constrained sphere. The cantilever was inclined to 11° in all cases to represent its angle during AFM measurement.

The influence of substrate material on cantilever bending shape was shown by side profiling the cantilever during indentation of glass (Figure 6b)) and silicone (Figure 6c)). Confocal reflection microscopy was used to create z-stacks of the cantilever (the attached sphere is not shown in Figure 6 for clarity). A clear difference in the cantilever bending profile for glass and silicone is evident even though the cantilever deflection (δ) is identical

for both materials. The cantilever bending profile against glass appears similar to that of a free ended cantilever and is comparable to that shown in Figure 5 suggesting sphere sliding is not inhibited by the glass substrate. The cantilever bending profile for silicone suggests the sphere is constrained, thus constraining rotation of the end of the cantilever (similar to the SEM image in Figure 5d)). This difference in bending profile would result in the photodetector measuring a larger change in voltage (slope change) for a glass substrate (Figure 6b)) than for a silicone substrate (Figure 6c)) even though the actual deflection (δ) is identical for both. Therefore, the conversion of measured voltage change (slope) to cantilever deflection is not applicable when sphere constraining occurs; as this conversion is based on the assumption of a free ended cantilever.

As it was not possible to characterize the bending profile of the cantilever during the course of an AFM experiment, here we propose that monitoring of the horizontal displacement of the sphere during indentation will indicate if sphere constraining occurs. Image analysis (ImageJ, National Institutes of Health, USA) of the spheres front edge during substrate loading in PBS found that 1 μm of cantilever z-displacement resulted in sphere forward displacement of $0.61 \pm 0.03 \mu\text{m}$ for glass (n=5). In contrast, no detectable sphere forward displacement ($0.04 \pm 0.08 \mu\text{m}$) was observed for a silicone substrate (n=5).

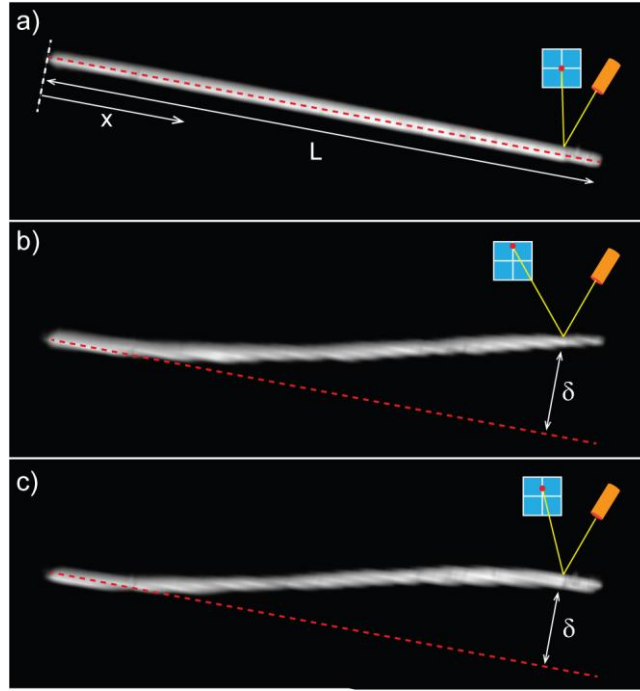


FIG 6. Side profiling of a cantilever a) not in contact with a substrate, b) in contact with glass (sliding sphere profile) and c) in contact with silicone (constrained sphere profile). Images are created from z-stacks captured using confocal reflection microscopy (attached sphere not visible). This required loading to be performed outside of the AFM using a micromanipulator setup. The superimposed schematic of an AFM laser beam and photodetector illustrates that a larger change in voltage (slope change) would be measured for the sliding sphere profile b) than for the constrained sphere profile c) even though deflection (δ) is the same in each case. The cantilever is length L with axial position x .

C. Correction of force-indentation measurements

It has been demonstrated that the cantilever does not act as a free ended beam when sphere constraining occurs. A constrained sphere applies an additional torque at the leading edge of the cantilever and thus affects AFM measurements in two ways:

- (i) The conversion of measured slope to reported deflection does not follow that of a conventional AFM where free rotation of the cantilever is assumed. As will be demonstrated in the following, the determination of an appropriate correction factor is dependent on laser spot positioning on the cantilever.

- (ii) The force-deflection relationship changes. Rotation at the cantilevers leading edge is prevented by a constrained sphere, resulting in a cantilevering of the beam at both ends. Hence the spring constant of an equivalent free ended cantilever cannot be used to convert deflection to applied force.

Accounting for these relationship changes is vital for accurate determination of AFM measurements for a constrained sphere, i.e. when standard calibration for a sliding sphere scenario (e.g. OLS calibration on glass) is no longer sufficient. Here, we describe the steps required to correctly determine AFM measurements for the case of a constrained sphere.

(i) Relationship between measured slope and cantilever deflection

Conversion of the reported change in voltage from the photodiode to the actual cantilever deflection is dependent upon identifying whether a constrained sphere or a sliding sphere case is present. Again, this is due to the difference in slope along the cantilever for these two conditions, as shown in Figure 6. A sliding sphere allows the cantilever to behave as a free ended beam, whereas a constrained sphere results in a beam that has rotation fully constrained at both ends. The forward displacement of the sphere was shown above to be negligible compared to the z-displacement of the cantilever; therefore, as there is sufficient friction between the sphere and substrate, rotation of the end of the cantilever is fully constrained, as indicated in Figure 6. Analytical solutions from simple beam theory are used to compute the slope profiles along the axis of a cantilever (Figure 7a)) when identical end deflections are imposed in both cases. Finite element simulations were used to verify these results. Clearly, the difference in slope between the constrained and sliding sphere is a function of axial position (x) along a cantilever of length L . Only at a cantilever position of $x/L = 0.66$ is the slope identical for both cases. The ratio of sliding slope to constrained slope is shown in Figure 7b). It can be observed that the slope ratio is highly sensitive to axial position near the leading edge of the cantilever ($x/L > 0.9$).

As demonstrated in Figure 7, in order to determine the correct deflection for the case of a constrained sphere, it is essential that the laser spot position on the cantilever is known. In this study, an optimum laser spot position of $x/L=0.8$ was chosen. This position was selected as a compromise between the maximum OLS at the leading edge of a cantilever for the sliding sphere (i.e. during calibration on glass) and the maximum OLS at the middle of the cantilever for the constrained sphere (e.g. during subsequent experimental measurement of cells or silicone). At $x/L = 0.8$ a constrained sphere profile will result in the measurement of a slope that is 1.5 times lower than the slope that would be measured at this position for a sliding sphere with an identical end deflection (as indicated by the dashed line in Figure 7b)). Therefore, in cases where sphere constraining occurs, when the laser spot position is at $x/L = 0.8$, a correction factor of 1.5 must be applied to the default AFM deflection measurement in order to obtain the correct deflection.

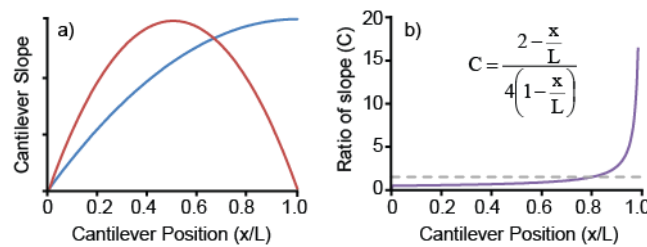


FIG 7. a) Cantilever slope along the axis of a cantilever which has a sliding sphere (blue) and constrained sphere (red) bending profile. Identical end deflections are imposed in each case. b) At a cantilever position of $x/L = 0.8$ the difference in slope is $\times 1.5$ (dashed line). Inset: correction factor for slope as a function of axial position along the cantilever (x/L).

(ii) Force-deflection relationship

The force-deflection relationship differs for a sliding sphere and for a constrained sphere. As discussed above, simple beam theory allows the sliding sphere case to behave as a free ended beam and the constrained sphere case to behave as a beam with rotation fully constrained at both ends. Therefore, the correction factor that accounts for the different force-deflection relationship may be determined by comparing the analytical solutions for identical

beam deflections for constrained and sliding beams. Hence, the force applied by the cantilever is four times higher for the constrained case:

$$\delta_{constrained} = \delta_{sliding}$$

$$\frac{F_{constrained}L^3}{12EI} = \frac{F_{sliding}L^3}{3EI}$$

$$F_{constrained} = 4F_{sliding}$$

In summary, to correctly determine the deflection and force measured for the case of a constrained sphere, the slope change recorded by the AFM has to be corrected according to Figure 7b) and is only dependent on the relative axial position of the laser spot along the cantilever. In our experiments, the laser is positioned at $x/L = 0.8$, therefore a slope-deflection correction factor of x1.5 is implemented. Due to rotation constraint at the cantilever leading edge, the cantilever stiffness is four times higher than that of a free ended cantilever.

Validation of the slope-deflection and force-deflection relationship changes was achieved by indenting silicone of a known elastic modulus. The OLS was calibrated on glass in PBS. Force-deformation measurements were performed on the silicone in PBS at 5 separate locations. Figure 8 shows the force (mean \pm standard deviation) at 10 sample indentation depths for both the uncorrected and corrected data. The uncorrected default AFM data reports a maximum force of $0.48 \pm 0.08 \mu\text{N}$ at an indentation of $0.9 \mu\text{m}$. This resulted in a calculated elastic modulus of 0.05 MPa . Application of the correction factors determined above to the data results in a maximum force of $2.88 \pm 0.47 \mu\text{N}$ at a corrected indentation depth of $0.4 \mu\text{m}$. This resulted in an 18 fold increase in elastic modulus of 0.94 MPa .

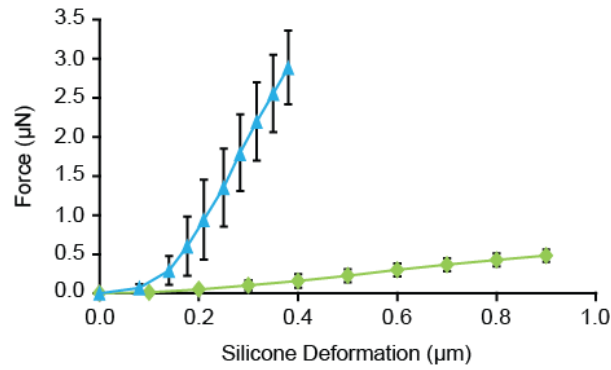


FIG 8. Uncorrected (green) and corrected (blue) AFM force-deformation data. The elastic moduli were calculated as 0.05 MPa and 0.94 MPa, respectively.

Tensile testing (0-10 % strain) of four sections of the silicone substrate indicated the elastic modulus to be 0.92 ± 0.08 MPa, which was within 2 % of the corrected AFM data. The uncorrected AFM data resulted in a substantial (18 fold) underestimation of the silicone's elastic modulus. This highlights the significant error that can arise when a changing cantilever bending profile is not considered and illustrates the necessity of careful interpretation of reported AFM measurements.

Previous studies have attempted to account for the effects of altered cantilever bending. A theoretical paper by Edwards *et al.* developed correction factors to account for the effects of cantilever tilt and induced torque on force measurements.³⁸ Furthermore, Evans *et al.* described equations to determine cantilever deflection for different loading scenarios.³⁹ However, to the authors' knowledge, the current paper presents for the first time, a practical methodology that accounts for *both* the altered cantilever stiffness and altered deflection to correctly determine AFM force-indentation measurements when cantilever bending is altered by constraining during contact. The methodology described here requires only the monitoring of the forward displacement of the sphere during loading in order to determine whether constraining occurs and therefore decide whether the correction factors are applied. Failure to apply the correction factors for the case of a constrained sphere will have a significant impact on the force-indentation measurements reported.

IV. APPLICATION OF DISPLACEMENT CONTROLLED AFM TO WHOLE CELL MECHANICS

Displacement controlled AFM has a number of potential applications, in particular in the field of cell mechanics. Here, we demonstrate this system to investigate the effects of cyclic deformation, directly comparable to the macroscale study by Wille *et al.* The key requirements are continuous uninterrupted cyclic cell deformation (constant strain rate) and uniform loading of the cell (whole cell deformation).

It is important to note that a comprehensive single cell investigation is beyond the scope of the present paper and will be presented in a follow-on article. Here we simply demonstrate that the stabilized system developed in this study must be used for single cell strain controlled cyclic deformation and highlight the significant errors that can occur in applied cell strain when an unmodified system is used.

A. Unmodified versus modified system

To highlight the importance of precise displacement control, cyclic cell deformation was performed for both an unmodified (open GBPD and no temperature control) and modified system. MC3T3-E1 osteoblasts (ATCC-LGC Standards, UK) were cultured according to the method described by McGarry *et al.*²⁶ Suspended cells in PBS were injected into the fluid cell via the inlet tube valve through the side portal window of hood. An additional 10 minutes was allowed for cell attachment to the glass substrate and system equilibration. The initial cell height was determined by force-displacement curves as the difference between the glass substrate and the cell. Phase contrast optical microscopy allowed aligning of the microsphere above the center of the cell, Figure 9. The cell was then subjected to cyclic compression from 0 % to 25 % deformation (relative to initial cell height) at a frequency of 0.1 Hz for a period of 36 minutes.

Accurate determination of the cell deformation data required knowledge of the cantilever bending profile during cell indentation. Inspection of the sphere during 2 μm cell indentation showed the sphere did not move forward ($0.00 \pm 0.13 \mu\text{m}$) and therefore sphere constraining occurred ($n=5$). Consequently, all force data reported here was corrected using the factors identified in Section III(c). However as the cells used in this study have an elastic modulus no higher than 7 kPa⁴⁰ it was not necessary to apply an indentation depth correction, since the deflection is much smaller than the piezo z-displacement for these experiments.

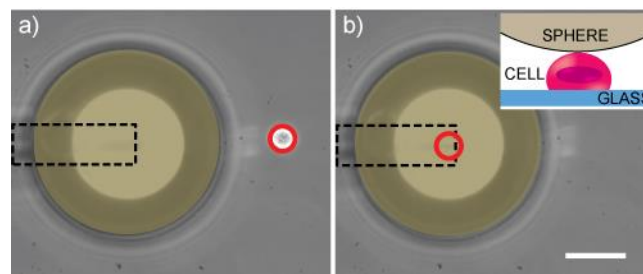


FIG. 9. Bottom-view phase contrast images of the modified cantilever, showing outline of tipless cantilever (dashed), attached sphere (brown), and a cell adhered to the glass substrate (red circle). a) shows the modified cantilever beside a cell, and b) centered above the same cell. Inset: schematic representation of sphere in contact with the top of the cell. Scale bar = 50 μm .

Figure 10(a, b) shows the minimum force, recorded at the beginning of each cycle (0 % compression) and the maximum force recorded at the mid-point of each cycle (25 % compression) for the unmodified and modified system. The initial minimum force (3.0 nN) for the unmodified system decreases by 9 nN over the first 2 cycles compared to an initial minimum force (15.6 nN) for the modified system decreasing by 10.2 nN over the first 5 cycles. Following this rapid decrease, the rate of reduction is 7.8 times larger for the unmodified system compared to the modified system.

Regarding the maximum force, the initial values are 120.6 nN and 75.0 nN for the unmodified and modified systems, respectively. Both systems exhibited an initial decrease within the first 10 cycles of compression. Following a local minimum, the force in the

unmodified system steadily increases in subsequent cycles, reaching a value of 175.8 nN following 36 minutes. In contrast, for the modified system the measured force reaches a steady state value of 70.2 nN following 22 minutes of cyclic deformation. It should also be noted that spikes in maximum force are observed for the cell within the unmodified system. From force-displacement curves taken on the substrate before and after each experiment the z-drift value can be obtained, Table I. The sphere-surface distance decreased by 1.50 μm for the unmodified system versus 0.02 μm for the modified system, as shown in Figure 10(g). This resulted in an actual cell indentation (relative to the initial cell height) of 40.95 % for the unmodified system, compared to the desired value of 25 %. In contrast, a value of 25.26 % was achieved using the modified system.

In Figure 10 the first (c, d) and last (e, f) cell deformation cycles for each system are also shown. For both systems the first cycle shows a non-linear increase in force during compression. Hysteresis is observed during the unloading half of the cycle. For both systems the force value at the end of the cycle is lower than the starting point. The final cycle at 36 minutes reveals significant differences between the modified and unmodified system. In the unmodified system, the final cycle (e) starts at a negative force (~ -42 nN). During the early stages of the loading half-cycle the force rapidly increases to a value of 0 nN. This is followed by an intermittent plateau at ~ 0 nN, followed by further force increase to a peak value of 175.8 nN. In comparison the last cycle (f) in the modified system starts at 0.6 nN, beginning with a rapid increase in force and then continuing along a similar force-strain curve to that observed for the first cycle.

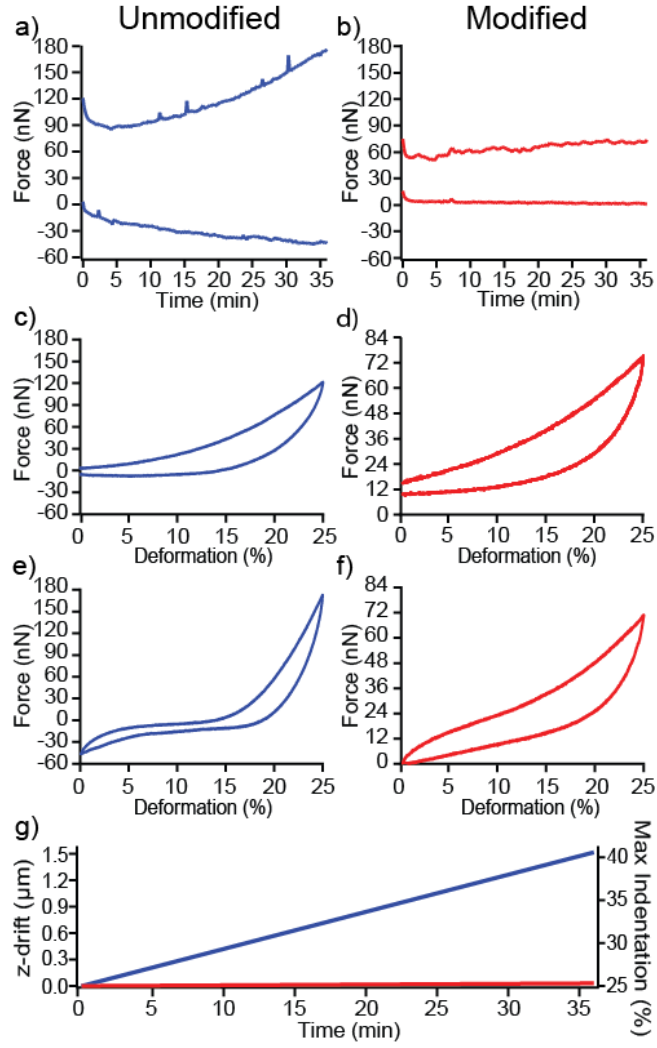


FIG. 10. Single cell cyclic deformation experiment from 0 - 25 % of its original cell height at a frequency of 0.1 Hz using a \varnothing 150 μm sphere within an unmodified (blue) and modified (red) system. For each system, (a, b) the minimum force (at 0 % deformation) and maximum force (at 25 % deformation) is shown. The first (c, d) and last (e, f) cycles during cell deformation for both systems is also highlighted. (g) A linear interpolation of z-drift and maximum indentation (relative to original cell height) is also shown. All force data is corrected for baseline deflection drift between the start of and end of the experiment (linearly interpolated).

TABLE I. Comparison of cell cyclic deformation for an unmodified and modified system

System setup	Initial cell height	Initial cell diameter ($\pm 1.6 \mu\text{m}$)	Sphere-surface distance change	Change in indentation depth
Unmodified	9.4 μm	17.1 μm	1.50 μm	15.96 %
Modified	9.4 μm	18.0 μm	0.02 μm	0.26 %

The trend observed for the unmodified system, whereby the maximum force continuously increases, significantly differs from the findings of Wille *et al.*, in which cyclic stretching of a large population of cells in a collagen scaffold results in a steady state cell force following ~30 minutes of stretching.³ For the unmodified system considered in the present study the continuous increase in force occurs due a continuously increasing level of cell compression, from 25 % at the start of the experiment to ~41 % at the end of the experiment, due to z-drift. Additionally, the increasingly negative minimum forces obtained for the unmodified system indicates the cell is being stretched at the upper end of the deformation cycle, suggesting that the passive viscoelastic behavior of the cell begins to dominate the response of the cell at such elevated applied strains (20 % higher than the desired level). Clearly the forces measured using the unmodified system are dominated by the influence of z-drift, preventing reliable measurement of active force changes due to cytoskeletal remodeling.

The force profile obtained using the modified system contrasts sharply with data presented for an unmodified system. For the modified system, the initial decrease in maximum forces observed is characteristic of passive viscoelastic component of the cell material. However, the increase in maximum force to a steady state during the subsequent 22 minutes of cycling cannot be explained in terms of cell viscoelasticity. It is suggested that this slight increase in force is a result of remodeling of the cell actin cytoskeleton in response to cyclic deformation.⁴ The data presented are similar to a broad pattern of behavior previously observed for cells cyclically stretched at 0.1 Hz within a collagen matrix.³ In that study, isolation of the force contribution of the actin cytoskeleton from the total measured force revealed initial viscoelastic force reductions followed by slight force increases to a steady state following 30 minutes of cycling.

Analysis of individual force-deformation cycles reveals that a rapid increase in force occurs during the initial stages of the loading half cycle throughout the test (Figure 10(c-f)). If contact would have been broken during the unloading half cycles, the initial stages of the subsequent loading cycles would exhibit a run-in region of zero force until contact was established. This behavior was not observed in either the modified or unmodified system, demonstrating that the cell is in contact with the sphere at all times during the experiments. Phase contrast images were taken every 100 seconds and indicated that the cells under investigation remained centered under the sphere and did not significantly change from their original diameters ($\pm 1.6 \mu\text{m}$ limited by optical resolution), Table I. It would be expected that adherent cells such as these would generally spread to a diameter in excess of $40 \mu\text{m}$ during a 36 minute time period, as was observed for adjacent non-deformed cells. It is believed the constant cyclic deformation inhibited the cell spreading process. It is suggested that the remodeling of the actin cytoskeleton in response to applied cyclic strain inhibited its contribution to the spreading process.

A full investigation of the active cell forces during cyclic deformation is beyond the scope of this paper but the initial data presented here indicates that the displacement controlled technique represents an ideal single cell alternative to a microplate system to study cytoskeletal remodeling over long time scales, allowing precise force measurement and accurate control of cell strain and cell strain rate. With this long term stable system we have the ability to apply precise mechanical stimulation and accurately monitor the evolution of cell forces while simultaneously observing the cytoskeletal dynamics via optical techniques e.g. fluorescent microscopy (epi-/confocal). Additionally, the role of cytoskeletal remodeling in cell spreading will also be investigated using this system, given that initial results suggest that cyclic stretching affects the dynamic process of cell spreading.

V. CONCLUSION

In summary, we have developed a readily implementable, cost effective method of modifying an AFM for z-displacement controlled operation in both air and liquid over long timescales. For operation in air, we demonstrated that after 5 hours of equilibration, the z-drift for the unmodified system was 111.56 ± 112.97 nm/hr compared to 9.28 ± 5.41 nm/hr for the modified system. This represents over a 10 fold improvement in performance in air whilst not significantly altering the system stability (4.62 ± 1.08 nm unmodified, 4.94 ± 0.46 nm modified). For operation in fluid, it was demonstrated that z-drift remains within 31.67 ± 19.49 nm over a period of 5 hours. This represents a maximum of 0.34 % error in indentation depth due to z-drift for a cell 15 μm high.

This study demonstrates the importance of eliminating thermal drift for all AFM studies on long timescales where continuous accurate knowledge of the tip-sample separation is required and cannot be obtained using conventional methods. Whilst specialized commercial systems are currently available that offer similar z-drift stability, our method of achieving displacement control can be readily implemented on existing AFM systems. Displacement controlled AFM has many applications including nano-manipulation, dynamic behavior monitoring, and deformation controlled measurements.

Whole cell deformation was achieved by attaching a large sphere to a cantilever in order to approximate a parallel plate configuration. It was found that careful reinterpretation of reported AFM data was required to account for sphere constraining. Sphere constraining applies an additional torque to the cantilever leading edge and thus changes the slope-deflection and force-deflection relationships used in optical lever systems. By applying the methodology presented in this study it is possible to correctly determine force and indentation where the cantilever is considered to be either a free ended beam (e.g. OLS on glass) or a beam with a constrained contact (as was the case for our cell indentation measurements).

Combining these readily implementable methods of performing whole cell deformation with our displacement controlled AFM setup we obtained preliminary data which demonstrates the potential of our system to investigate the biomechanical response to long term cyclic loading of whole cells.

ACKNOWLEDGEMENTS

This work was supported by Science Foundation Ireland (Grant Nos. 08/RFP/ENM1726 and 07/INI/B931) and the Higher Education Authority's Programme for Research in Third-Level Institutions (PRTL15 Nanoremedies).

REFERENCES

- 1 R. Kaunas, P. Nguyen, S. Usami and S. Chien, Proc. Natl. Acad. Sci. **102**, 15895 (2005)
- 2 J. H. C. Wang, P. Goldschmidt-Clermont, J. Wille and F. C. P. Yin, J. Biomech. **34**, 1563 (2001)
- 3 J. J. Wille, E. L. Elson and R. J. Okamoto, Ann. Biomed. Eng. **34**, 1678 (2006)
- 4 J. P. McGarry, A. G. Evans, R. M. McMeeking and V. S. Deshpande, *Proceedings of the ASME Summer Bioengineering Conference*, Resort at Squaw Creek, Lake Tahoe, California, 2009, p. 101
- 5 O. Thoumine, A. Ott, O. Cardoso and J. J. Meister, J. Biochem. Biophys. Meth. **39**, 47 (1999)
- 6 G. Ofek, D. C. Wiltz and K. A. Athanasiou, Biophys. J. **97**, 1873 (2009)
- 7 E. A. G. Peeters, C. W. J. Oomens, C. V. C. Bouten, D. L. Bader and F. P. T. Baaijens, J. Biomech. **38**, 1685 (2005)
- 8 B. Mokaberi and A. A. G. Requicha, IEEE Trans. Contr. Syst. Technol. **3**, 199 (2006)
- 9 J. H. Kindt, J. B. Thompson, M. B. Viani and P. K. Hansma, Rev. Sci. Instrum. **73**, 2305 (2002)
- 10 F. Oulevey, G. Gremaud, A. J. Kulik and B. Guisolan, Rev. Sci. Instrum. **70**, 1889 (1999)
- 11 C. Spagnoli, A. Beyder, S. R. Besch and F. Sachs, Rev. Sci. Instrum. **78**, 036111 (2007)
- 12 J. L. Choy, S. H. Parekh, O. Chaudhuri, A. P. Liu, C. Bustamante, M. J. Footer, J. A. Theriot and D. A. Fletcher, Rev. Sci. Instrum. **78**, 043711 (2007)
- 13 S. M. Altmann, P. F. Lenne and J. K. H. Hörber, Rev. Sci. Instrum. **72**, 142 (2001)
- 14 G. Schitter and A. Stemmer, Nanotechnology **13**, 663 (2002)
- 15 A. W. Sparks and S. R. Manalis, Appl. Phys. Lett. **85**, 3929 (2004)
- 16 M. S. Hoogeman, D. G. van Loon, R. W. M. Loos, H. G. Ficke, E. De Haas, J. J. van der Linden, H. Zeijlemaker, L. Kuipers, M. F. Chang and M. A. J. Klik, Rev. Sci. Instrum. **69**, 2072 (1998)
- 17 H. Torun, O. Finkler and F. L. Degertekin, Rev. Sci. Instrum. **80**, 076103 (2009)
- 18 Park Systems (www.parkafm.com); Agilent Technologies (www.agilent.com); Nanosurf (www.nanosurf.com)
- 19 THead (www.ntmdt.com); Dimension Edge (www.bruker-axs.com); Cypher (www.asylumresearch.com)
- 20 J. N. Munday, F. Capasso and V. A. Parsegian, Nature **457**, 170 (2009)
- 21 S. Zepeda, Y. Yeh and C. A. Orme, Rev. Sci. Instrum. **72**, 4159 (2001)
- 22 A. L. Rachlin, G. S. Henderson and M. C. Goh, Amer. Mineral. **77**, 904 (1992)
- 23 Y. Gan, Surf. Sci. Rep. **64**, 99 (2009)
- 24 See supplementary material at [] for additional liquid instability tests
- 25 G. T. Charras and M. A. Horton, Biophys. J. **82**, 2970 (2002)

- 26 J. G. McGarry, P. Maguire, V. A. Campbell, B. C. O'Connell, P. J.
Prendergast and S. P. Jarvis, *J. Orthop. Res.* **26**, 513 (2008)
- 27 H. J. Butt, *Biophys. J.* **60**, 1438 (1991)
- 28 W. A. Ducker, T. J. Senden and R. M. Pashley, *Nature* **353**, 239 (1991)
- 29 V. Lulevich, T. Zink, H. Y. Chen, F. T. Liu and G. Liu, *Langmuir* **22**, 8151
(2006)
- 30 P. P. Lehenkari, G. T. Charras, A. Nykänen and M. A. Horton,
Ultramicroscopy **82**, 289 (2000)
- 31 T. H. Fan and A. G. Fedorov, *Langmuir* **19**, 1347 (2003)
- 32 P. Attard, *J. Phys. Condens. Matter.* **19**, (2007)
- 33 H. J. Butt and M. Jaschke, *Nanotechnology* **6**, 1 (1995)
- 34 J. P. Cleveland, S. Manne, D. Bocek and P. K. Hansma, *Rev. Sci. Instrum.*
64, 403 (1993)
- 35 J. Stiernstedt, M. W. Rutland and P. Attard, *Rev. Sci. Instrum.* **76**, 083710
(2005)
- 36 K. H. Chung, G. A. Shaw and J. R. Pratt, *Rev. Sci. Instrum.* **80**, 065107
(2009)
- 37 J. H. Hoh and A. Engel, *Langmuir* **9**, 3310 (1993)
- 38 S. A. Edwards, W. A. Ducker and J. E. Sader, *J. Appl. Phys.* **103**, 064513
(2008)
- 39 D. R. Evans and V. S. J. Craig, *J. Phys. Chem. B* **110**, 5450 (2006)
- 40 G. M. Kelly, J. I. Kilpatrick, M. H. van Es, P. P. Weafer, P. J. Prendergast
and S. P. Jarvis, *J. Biomech.* **44**, 1484 (2011)